



N- and S-codoped graphene hollow nanoballs as an efficient Pt-free electrocatalyst for dye-sensitized solar cells

Yu-Ching Chang^{a,1}, Chi-Ang Tseng^{a,1}, Chuan-Pei Lee^{b,1}, Shiu-an-Bai Ann^c, Yi-June Huang^c, Kuo-Chuan Ho^c, Yit-Tsong Chen^{a,d,*}

^a Department of Chemistry, National Taiwan University, No. 1, Sec. 4, Roosevelt Road, Taipei, 106, Taiwan

^b Department of Applied Physics and Chemistry, University of Taipei, Taipei, 10048, Taiwan

^c Department of Chemical Engineering, National Taiwan University, Taipei, 10617, Taiwan

^d Institute of Atomic and Molecular Sciences, Academia Sinica, P.O. Box 23-166, Taipei, 106, Taiwan

HIGHLIGHTS

- N,S-codoped graphene hollow nanoballs (N,S-GHBs) are investigated for DSSCs.
- Highly curved GHBs provide high surface areas and sufficient active sites.
- N,S-GHBs enhance electrocatalytic activity toward the triiodide reduction reaction.
- DSSCs with a counter electrode of N,S-GHBs exhibit excellent device efficiency.

ARTICLE INFO

Keywords:

Chemical vapor deposition
Dye-sensitized solar cell
Graphene hollow ball
Heteroatom-doping
Pt-free counter electrode

ABSTRACT

We synthesize heteroatoms-doped graphene hollow nanoballs (GHBs) on flexible carbon cloth (CC) substrates via chemical vapor deposition (CVD) reaction to be used as an efficient non-noble electrocatalyst in dye-sensitized solar cells (DSSCs). The as-synthesized heteroatoms-doped GHBs/CC, including nitrogen-doped GHBs, sulfur-doped GHBs, and nitrogen and sulfur-codoped GHBs (denoted by N-GHBs/CC, S-GHBs/CC and N,S-GHBs/CC, respectively), are used as an efficient counter electrode (CE) in DSSCs. Unlike planar graphene sheets, the highly curved GHBs can avoid self-assembly restacking to provide high surface areas for electrocatalytic reactions. In addition, the heteroatomic incorporation in GHBs can reduce the charge-transfer resistance to enhance the electrocatalytic activity. Among these doped GHB samples, N,S-GHBs show the best catalytic performance due to the synergistic effect from both electronic and geometric changes, caused by the N- and S-dopings, respectively. The DSSC with a N,S-GHB CE exhibits the power conversion efficiency of 9.02%, comparable to that (8.90%) of a Pt-based counterpart.

1. Introduction

In recent years, dye-sensitized solar cells (DSSCs) have attracted great attention to be a promising alternative to traditional silicon-based solar cells, because of the advantages of DSSCs in semi-transparent visibility, simple and low-costly device fabrication, and relatively high conversion efficiency [1,2]. A typical DSSC consists of a dye-sensitized TiO₂ electrode, an electrolyte containing a redox couple, e.g., iodide/triiodide (I⁻/I₃⁻), and a counter electrode (CE). The CE plays a crucial role in promoting electron transfer from an external circuit back to the

electrolyte to regenerate the oxidized ionic species [3]. To date, platinum (Pt) has been widely used as an electrocatalytic CE in DSSCs by virtue of the high electronic conductivity and excellent catalytic activity of Pt in the redox reaction of I⁻/I₃⁻. However, Pt is a rare and expensive material and, most importantly, the unwanted formation of PtI₄ in the I⁻/I₃⁻-based electrolytic reactions [4–6] has limited Pt to hold long-term stability in DSSCs for large-scale commercial applications. Therefore, searching for cost-effective, earth-abundant, and stable electrocatalytic materials as a CE to replace Pt in DSSCs is an urgent challenge. Several Pt-free alternatives have been explored, such as non-Pt metals, transition

* Corresponding author. Department of Chemistry, National Taiwan University, No. 1, Sec. 4, Roosevelt Road, Taipei, 106, Taiwan.

E-mail address: ytchem@ntu.edu.tw (Y.-T. Chen).

¹ These authors contributed equally.

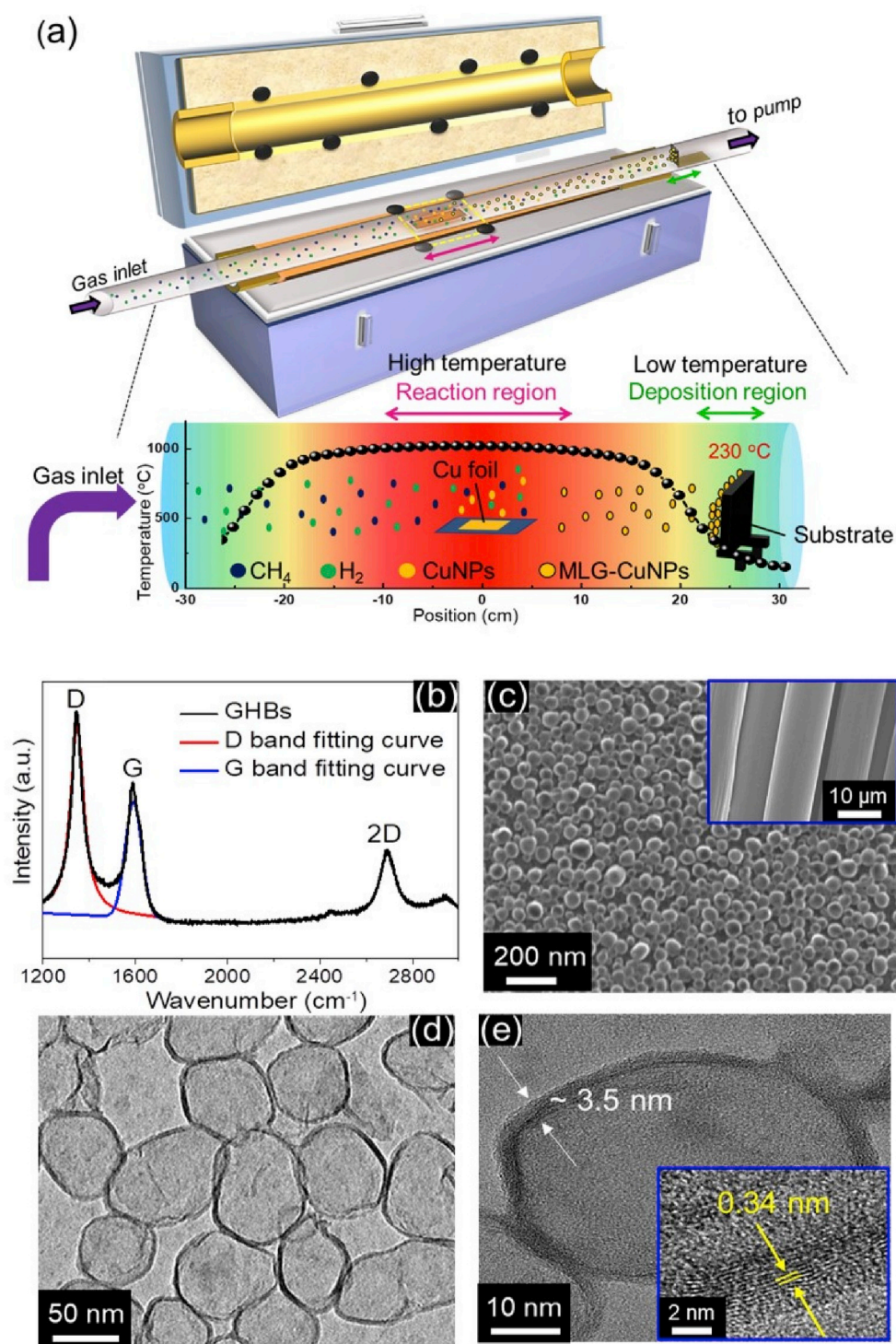


Fig. 1. (a) A schematic illustration represents the growth of GHBs on CC in a CVD reaction at 1090 °C. The temperature profile inside the quartz tube of the CVD system was measured with a thermocouple. (b) Raman spectrum of GHBs was observed with the laser excitation at 488 nm. (c) The morphology of the as-grown GHBs/CC was investigated with low-magnification (in the inset) and high-magnification SEM images. The detailed structure of GHBs, examined by (d) TEM and (e) HR-TEM, reveals the shell thickness (~3.5 nm) of a GHB with the lattice spacing of 3.4 Å between the graphene layers.

metallic compounds, conducting polymer, and carbon-based materials, of which the last include graphene, graphene oxide, reduced graphene oxide, carbon nanofiber, activated carbon, and ordered mesoporous carbon [7,8]. Among these candidates, the carbon-based materials with their merits of low cost, high conductivity, and good chemical stability can be an ideal substitute for Pt [9,10].

Graphene, a two-dimensional (2D) one-atom-thick carbon material of hexagonal lattice, can be a promising noble-metal-free CE because of its unique properties of high carrier mobility, electrical conductivity, mechanical strength and flexibility, and chemical stability [11]. However, the active sites of pristine graphene are located mainly at the edges

of the basal plane, resulting in poor electrocatalytic ability [12,13]. Although several approaches have been reported to address this issue by converting the structure of graphene to 3D configurations [14–16], the electrocatalytic activity of graphene can be increased by creating active sites directly on the basal plane with heteroatomic dopants. Recently, the graphene samples doped by heteroatoms, e.g., oxygen [17], nitrogen [18], boron [19], sulfur [20], and phosphorous [21], have been investigated intensively. Among these samples, the N-doped graphene without damaging the graphitic structure, due to the similar sizes between the N and C atoms, could enhance free carrier density, electrical conductivity, and the electron transfer from N-doped active sites to the

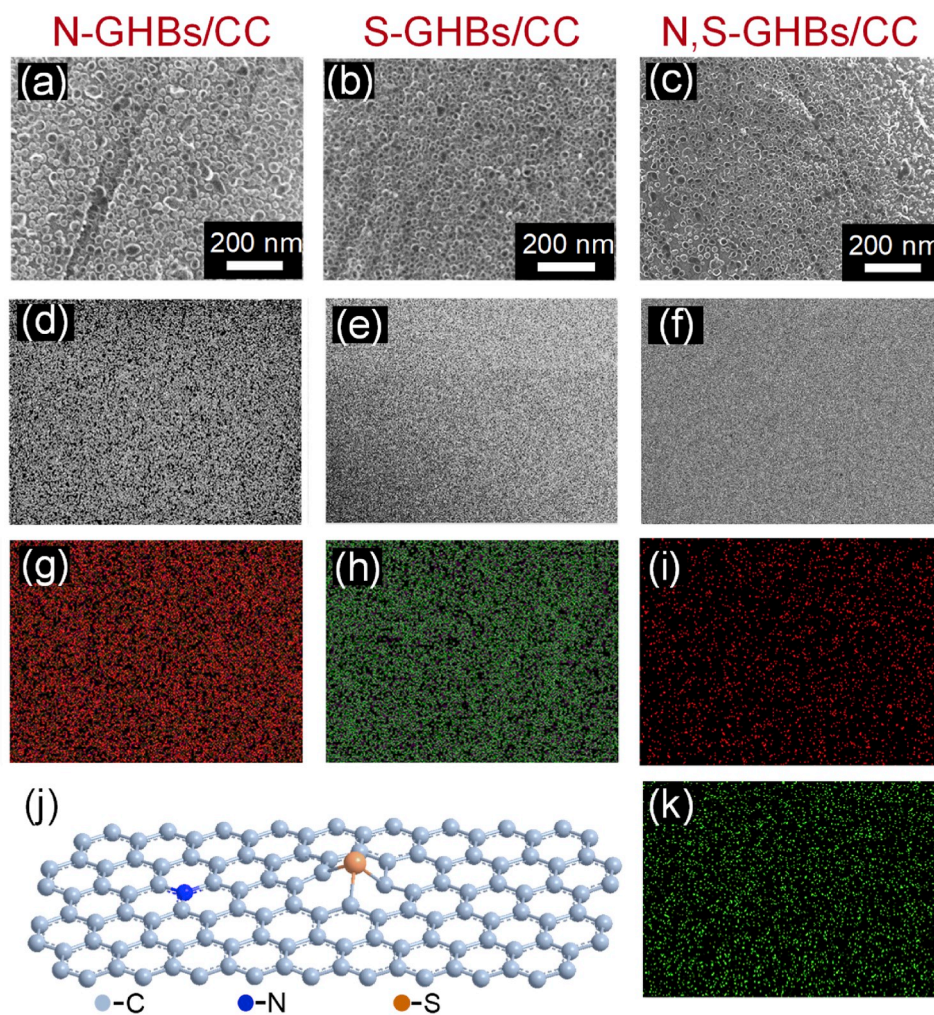


Fig. 2. The SEM images and elemental mappings of (a, d, g) N-GHBs/CC, (b, e, h) S-GHBs/CC, and (c, f, i, k) N,S-GHBs/CC. (j) A schematic illustration of the insertion of the N and S atoms into N,S-GHBs/CC is represented. While the embedding N dopants in the basal plane of graphene can generate an electronic effect because of the electronegative difference between the N and C atoms, the protruding S dopants from the graphene plane lead to a geometric effect due to a structural distortion.

adsorbed I_3^- in the redox reaction of I^-/I_3^- [12]. Comparatively, S-doped graphene, because of the much larger S than C in size, could cause geometric distortion to form the protruding S sites for effective adsorption of the I_3^- oxidizer. Consequently, it is interesting to develop the dual-doped graphene by N and S (denoted by N,S-Gr) as a new electrocatalyst in DSSCs [22]. Several theoretical calculations and experimental results have shown that a synergistic effect in the N,S-Gr was resulted from the asymmetric increase of charge densities at different sites of the dual-doped samples [12,23]. Compared with the single-doped graphene (by N or S), a dual-doped N,S-Gr can enhance both adsorptive and charge-transfer abilities toward the I_3^- reduction in DSSCs (*i.e.*, $I_3^- + 2e^- \rightarrow 3I^-$). The density functional theoretical (DFT) calculation [12] also reveals that N,S-Gr holds the advantages of controlling the charge density distribution, activating the inert sp^2 hybrid structure, and enhancing the catalytic ability on the basal plane of graphene.

In this study, we developed a chemical vapor deposition (CVD) method to synthesize heteroatoms-doped graphene hollow nanoballs (GHBs) directly on carbon cloth (CC) for the uses of an all-carbon CE in DSSCs. We synthesized nitrogen-doped graphene hollow nanoballs (N-GHBs), sulfur-doped graphene hollow nanoballs (S-GHBs), and nitrogen- and sulfur-codoped graphene hollow nanoballs (N,S-GHBs). The curved structure of GHBs can not only prevent graphene layers from stacking up to each other to enhance the surface areas [24], but also increase the defects on the graphene surface to create more active sites for easier

heteroatomic doping. Applying these heteroatoms-doped GHBs as different CEs in DSSCs, we compared their unique electrochemical characteristics. For a N-GHB CE, the doping of N atoms attracts electrons from the nearby C atoms and facilitates an easier electron transfer from the graphene surface to the adsorbed iodine molecule, thus reducing the charge-transfer resistance. On the other hand, the doping of S atoms in a S-GHB CE causes the local structural distortion of planar graphene to act as active sites for the more effective iodine adsorption. In combination, the synergistic effect in a N,S-GHB CE can not only reduce the charge-transfer resistance but also provide active sites, thereby greatly enhancing the catalytic activity in DSSCs. Consequently, the power conversion efficiency of a DSSC with a N,S-GHB CE can reach 9.02%, comparable to that (8.90%) of a standard sputtered Pt CE-based cell.

2. Results and discussion

As shown in Fig. 1a, GHBs were grown on CC in CVD reaction and the experimental procedures are described in Section S2 of the Supporting Information. An experimental advantage of this CVD design is that while the reaction of chemical precursors was conducted at the high-temperature zones (e.g., 1090 °C in this study), the synthesized GHB products could be deposited at the low-temperature region (~230 °C). With this architectural design, a variety of collection substrates (e.g., CC, polyimide film, silicon wafer, etc.) can be used to grow the CVD products [25], especially beneficial for a substrate that cannot stand for high

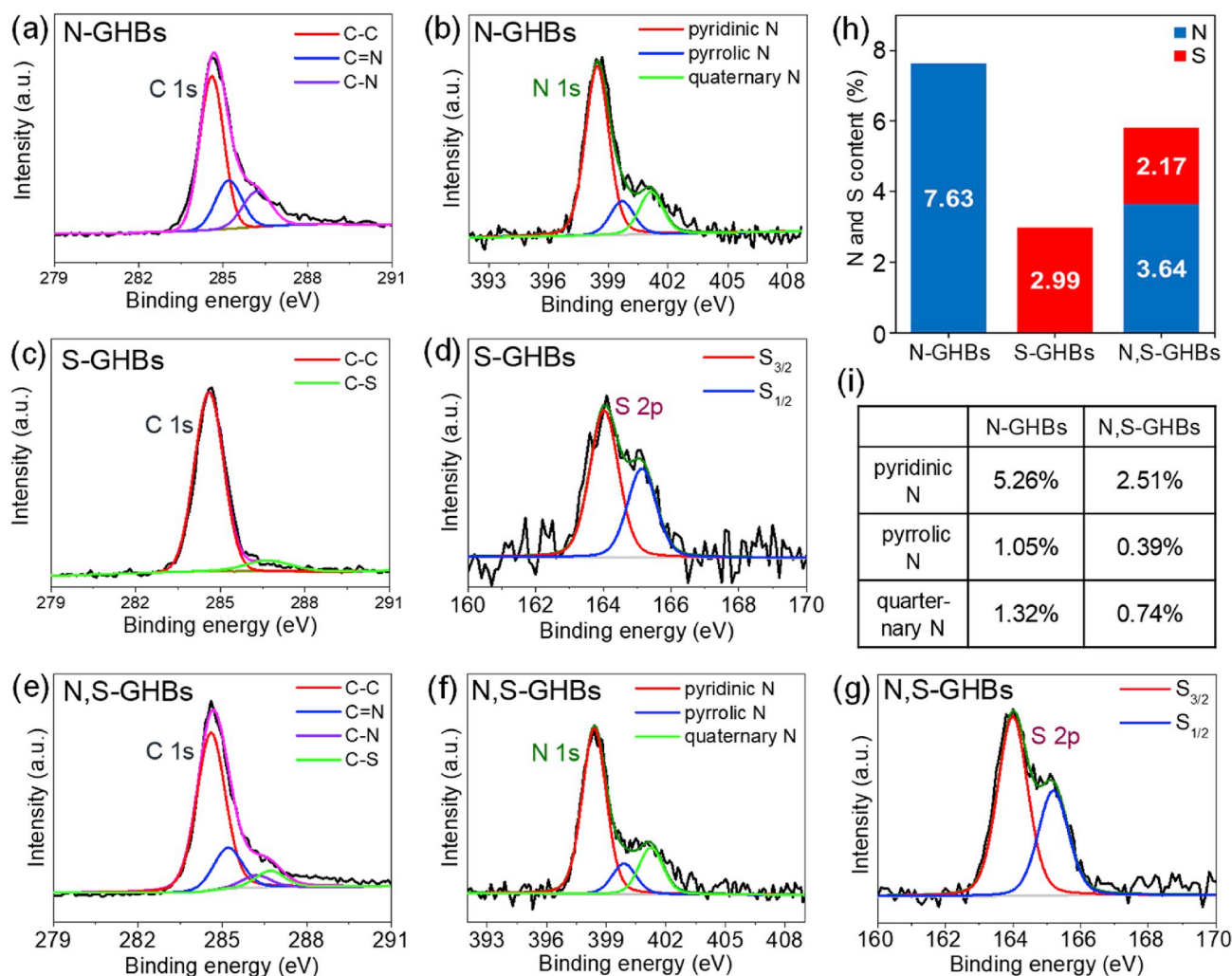


Fig. 3. The high-resolution XPS spectra of C 1s for (a) N-GHBs, (c) S-GHBs, and (e) N,S-GHBs show the signals of C=C at 284.6 eV, C=N at 285.1 eV, C-N at 286.2 eV, and C-S at 286.7 eV. The N 1s spectra of (b) N-GHBs and (f) N,S-GHBs indicate the bands of pyridinic N at 398.5 eV, pyrrolic N at 399.5 eV, and quaternary N at 401.2 eV. The S 2p spectra of (d) S-GHBs and (g) N,S-GHBs exhibit the signals of C-S $2p_{3/2}$ at 164.0 eV and C-S $2p_{1/2}$ at 165.1 eV. (h) The doping amounts of the N and S atoms in N-GHBs/CC, S-GHBs/CC, and N,S-GHBs/CC are displayed for comparison. (i) Different N-doped states are distributed in N-GHBs/CC and N,S-GHBs/CC. The analysis of doping levels from the observed XPS spectra is described in Section S6.2 of the Supporting Information.

temperature, such as a polyimide film. The Raman spectrum of highly-curved GHBs was observed as shown in Fig. 1b, where spectroscopic analysis reveals that GHBs contain many crystallite domains with an estimated size of ~ 9 nm (Section S3 of the Supporting Information). The spectrum shows three well-recognized D, G, and 2D bands at 1350, 1590, and 2690 cm^{-1} , respectively. The 2D band originates from a second-order inelastic scattering process to link electrons and phonons, where two phonons are involved near the K point of the dispersion relation of graphene [26]. The band at 2935 cm^{-1} corresponds to the D + G band, which is caused by the strain-induced effect of a non-planar graphitic structure [25]. The surface morphologies of GHBs/CC were characterized by scanning electron microscopy (SEM) with low- and high-magnifications (Fig. 1c), in which GHBs of 50–80 nm in size were grown uniformly on CC. Furthermore, the hollow spherical structure of GHBs was observed by transmission electron microscopy (TEM, Fig. 1d). Displayed in Fig. 1e are the high-resolution TEM (HR-TEM) images of the shell of a GHB (~ 3.5 nm in thickness), which corresponds to ca. 10 graphene layers with the lattice spacing of 3.4 Å between the graphene layers.

Graphene has high conductivity, chemical stability, and mechanical strength; however, pristine graphene shows low catalytic performance for the I_3^- reduction in DSSCs, because the active sites of graphene are

located mainly at the edges of the basal plane. Nevertheless, several studies have demonstrated that the insertion of heteroatoms into the basal plane could greatly enhance the electrocatalytic activity of graphene [27,28]. In line with the same reasoning, we synthesized nitrogen-doped, sulfur-doped, and nitrogen and sulfur-codoped GHBs on CC (represented by N-GHBs/CC, S-GHBs/CC, and N,S-GHBs/CC, respectively with the experimental details described in Section S2 of the Supporting Information) and examined their structural characteristics and electrocatalytic performances. The SEM images and elemental mappings of N-GHBs, S-GHBs, and N,S-GHBs are shown in Fig. 2, where spherical GHBs are spread uniformly on CC and the doped atoms of N and S are evenly distributed in GHBs, confirming that the successful introduction of the N and S atoms into GHBs.

In Fig. 3, we applied X-ray photoelectron spectroscopy (XPS) to investigate the chemical bondings and the doping amounts of the N and S atoms in the as-synthesized N-GHBs, S-GHBs, and N,S-GHBs. The high-resolution C 1s spectra of N-GHBs/CC (Fig. 3a), S-GHBs/CC (Fig. 3c), and N,S-GHBs/CC (Fig. 3e) reveal the characteristic bonds of C=C at 284.6 eV, C=N at 285.1 eV, C-N at 286.2 eV, and C-S at 286.7 eV [5, 29], indicating that the graphitic sp^2 C is dominant and the N and S heteroatoms are successfully incorporated into the graphene lattice. Furthermore, three different N-doped states of pyridinic N at 398.5 eV,

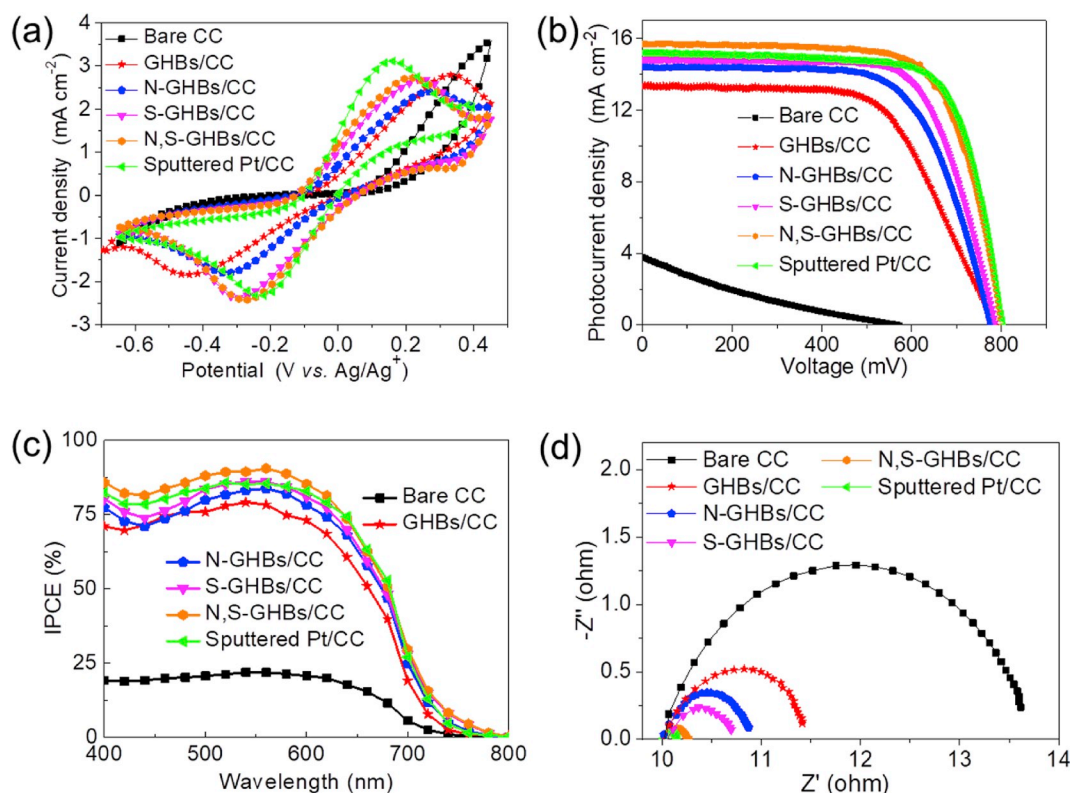


Fig. 4. The electrochemical activities were tested with the electrochemical cells containing various CEs of bare CC, GHBs/CC, N-GHBs/CC, S-GHBs/CC, N,S-GHBs/CC, and sputtered Pt/CC. The electrochemical measurements for these tests include (a) cyclic voltammograms, (b) photocurrent density vs. voltage (J - V , under AM 1.5G illumination at 100 mW cm^{-2}) curves, (c) incident photon-to-electron conversion efficiency (IPCE), and (d) electrochemical impedance spectra (EIS, under AM 1.5G illumination at 100 mW cm^{-2}).

Table 1

The electrochemical parameters of various CEs in a DSSC are compared.

Counter electrodes	J_{PC} , cathodic current density (mA cm^{-2})	ΔE_p , peak separation (mV)
Bare CC	N.A.	N.A.
GHBs/CC	-1.13	698
N-GHBs/CC	-1.41	530
S-GHBs/CC	-2.09	498
N,S-GHBs/CC	-2.22	459
Sputtered Pt/CC	-1.82	363

pyrrolic N at 399.5 eV, and quaternary N at 401.2 eV in both N-GHBs (Fig. 3b) and N,S-GHBs (Fig. 3f) were analyzed by deconvoluting the N 1s spectra [30] with their doping levels listed in Fig. 3h and i. The pyridinic N is the dominant configuration in both N-GHBs and N,S-GHBs (Fig. 3i), because the pyrrolic N is thermally less stable [31] and the formation of quaternary N requires much more energy than the other two N-doped states [32]. Finally, two different S-doped states of C-S $2p_{3/2}$ at 164.0 eV and C-S $2p_{1/2}$ at 165.1 eV in S-GHBs (Fig. 3d) and N,S-GHBs (Fig. 3g) were examined from the deconvoluted S 2p spectra [33] with their doping levels shown in Fig. 3h.

Next, we measured the electrocatalytic performance of different CEs in a three-electrode electrochemical system by comparing the heteroatoms-doped GHBs (including N-GHBs/CC, S-GHBs/CC, and N,S-GHBs/CC) with bare CC, GHBs/CC, and sputtered Pt/CC. The details of electrode preparations and electrochemical measurements are described in Sections S4–S6 of the Supporting Information. In DSSCs, a CE is responsible for the regeneration reaction of the I_3^- ions, i.e., $I_3^- + 2e^- \rightarrow 3I^-$. As shown in Fig. 4a, the electrocatalytic abilities of different CEs (including bare CC, GHBs/CC, N-GHBs/CC, S-GHBs/CC, N,S-GHBs/CC, and sputtered Pt/CC) were tested by cyclic voltammetry (CV). The

bare CC has extremely poor electrocatalytic activity, where barely any redox signals could be detected. As summarized in Table 1, the peak separation (ΔE_p) between the oxidation peak and reduction peak shows an order of GHBs/CC > N-GHBs/CC > S-GHBs/CC > N,S-GHBs/CC > sputtered Pt/CC, indicating the heteroatoms-doped GHBs required less overpotential to trigger the I_3^- reduction as compared with bare GHBs. Notably, with the insertion of both N and S atoms, the ΔE_p value for N,S-GHBs is further decreased and becomes closer to the ΔE_p value of a sputtered Pt/CC. The ΔE_p value varies inversely with the intrinsic heterogeneous rate constant, where a lower ΔE_p value represents a better charge-transfer kinetic process. On the other hand, the cathodic peak current density (J_{PC}), positively correlating with the electrochemically active area of an electrode, follows an order of N,S-GHBs/CC > S-GHBs/CC > sputtered Pt/CC > N-GHBs/CC > GHBs/CC (see Table 1). As a result, the N,S-GHBs/CC with an increasing number of active sites exhibits the best J_{PC} value among all of the electrode samples tested.

In addition, a recent simulation study indicates that N,S-Gr can improve electrocatalytic activity by the synergistic effect, which could be accounted for by the electronic and geometric factors. While the difference in electronegativity (χ) between the C atom ($\chi_C = 2.55$) and doped elements, i.e., N ($\chi_N = 3.04$) and S ($\chi_S = 2.58$), could generate an electronic effect, a mismatch of bond length (such as C–S vs. C–C) could create a geometric effect. In the I_3^- reduction reaction, Chen et al. [12] reported that the difference in electronegativity between C and the doped atom, such as N, will change the density of electron cloud of the C atom. The N atom attracts the electron clouds from nearby C atoms, promoting the electron transfer from N to the adsorbed iodine molecules. Moreover, after doping S atoms, the longer bond length of C–S (1.78 Å) than C–C (1.54 Å) will cause a structural distortion on the graphene surface and the nearest sp^2 C atom is pulled into an sp^3 C-like atom, which is easier to adsorb iodine molecules and acts as an active site for the I_3^- reduction. Consequently, the electrocatalytic properties of

Table 2

The photovoltaic parameters of various CEs in a DSSC are compared under AM 1.5G (100 mW cm⁻²) illumination.

Counter electrodes	η (%)	V_{oc} (mV)	J_{sc} (mA cm ⁻²)	FF	J_{IPCE} (mA cm ⁻²)
Bare CC	0.41	570	3.80	0.19	3.67
GHBs/CC	6.47	785	13.33	0.62	13.06
N-GHBs/CC	7.48	776	14.44	0.67	14.07
S-GHBs/CC	8.15	785	14.84	0.70	14.68
N,S-GHBs/CC	9.02	798	15.71	0.72	15.56
Sputtered Pt/CC	8.90	802	15.22	0.73	14.96
GHBs/CC ^a	6.20	697	14.50	0.61	14.29
N-GHBs-P3/CC ^a	7.53	703	16.09	0.67	15.99

^a From Ref. [30].

N,S-Gr can be well understood by the synergistic effect of combining the electronic and geometric factors.

The photocurrent density vs. voltage (J - V) curves of a DSSC with various CEs of bare CC, GHBs/CC, N-GHBs/CC, S-GHBs/CC, N,S-GHBs/CC, and sputtered Pt/CC are shown in Fig. 4a with the corresponding parameters tabulated in Table 2. We found that a DSSC with bare CC as a CE shows poor overall light-to-electricity conversion efficiency (η) of 0.41%. After decorating GHBs, the η of a GHBs/CC CE can be greatly enhanced to 6.47%. This enhancement is due to the strain-induced structural defects on the highly curved GHBs, which beneficially act as the active sites on the CE surface for electrocatalytic reactions; meanwhile, hollow GHBs could provide bifacial electrocatalytic surfaces, facilitating the charge transfer from CE to I₃⁻. By using the CEs of N-GHBs/CC, S-GHBs/CC, and N,S-GHBs/CC, the corresponding η can be further improved to 7.48%, 8.15%, and 9.02%, respectively, where the $\eta = 9.02\%$ of N,S-GHBs/CC is even slightly higher than that (8.90%) of a sputtered Pt/CC. A comparison of the DSSC performance between a N,S-GHBs/CC CE and previously reported electrodes is summarized in Table S1. It can be found that by employing different CEs of GHBs/CC, N-GHBs/CC, S-GHBs/CC, and N,S-GHBs/CC for the DSSC tests, the distinct efficiency originates mainly from the differences in short-circuit photocurrent density (J_{SC}) and fill factor (FF). With the same photoanode and electrolyte in a DSSC, a high J_{SC} may reflect the good electrocatalytic ability of a CE for the quick reduction of I₃⁻, which in turn can lead to the fast charge-transfer kinetics in the cell to reach a high FF . These mechanisms have been discussed in the above cyclic voltammetry (CV) analysis and will be further verified by electrochemical impedance spectroscopy (EIS). Fig. 4c shows the incident photon-to-electron conversion efficiency (IPCE) spectra of various DSSCs with different CEs. Each of the tested CEs exhibits a broad IPCE curve, covering the visible region from 400 to 800 nm, with the integrated photocurrent density (J_{IPCE}) summarized in Table 2 by integrating IPCE with the AM 1.5G solar spectrum. These J_{IPCE} values are in consistency with the corresponding J_{SC} values obtained from their photovoltaic performances (Fig. 4b and Table 2).

Finally, EIS was used to investigate the interfacial charge-transfer kinetics for the electrocatalytic electrodes, where a symmetric cell consisting of the same electrocatalyst on both anode and cathode was employed for tests. The FRA2 module was operated between 10 mHz and 100 kHz under an open-circuit condition with an AC amplitude of ± 10 mV. As shown in Fig. 4d, the semicircle corresponds to the charge-transfer resistance (R_{ct}) occurring at the electrocatalytic electrode/electrolyte interface; the smaller diameter of a semicircle represents the lower charge-transfer resistance during the electrocatalytic reaction. The R_{ct} values of various electrocatalytic electrodes show a tendency of N,S-GHBs/CC \approx sputtered Pt/CC < S-GHBs/CC < N-GHBs/CC < GHBs/CC < bare CC. A symmetric cell with the lower R_{ct} value implies the less loss of internal energy at the electrode/electrolyte interface during the electrocatalytic process; accordingly, the reduction reaction of I₃⁻ can work more efficiently at the electrocatalytic electrode. Consequently, it can be concluded that the lower charge-transfer resistance is responsible

for the greater performance of DSSCs.

3. Conclusion

We developed a CVD method to synthesize all-carbon N,S-GHBs/CC CEs to be used as an alternative to Pt in DSSCs. The highly curved GHBs with a 3D spherical configuration prevent planar graphene sheets from self-assembly restacking and provide high surface areas for electrochemical reactions. In addition, heteroatoms-doped GHBs can reduce the charge-transfer resistance in the I⁻/I₃⁻ redox reaction and enhance the catalytic activity of GHBs. Finally, the photovoltaic performance of N,S-GHBs was measured to reach 9.02%, comparable to that (8.90%) of a standard sputtered Pt CE-based cell.

Declaration of competing interest

The authors declare that they have no known competing financial interests or personal relationships that could have appeared to influence the work reported in this paper.

Acknowledgement

This work was supported, in part, by the Ministry of Science and Technology (MOST) of Taiwan under Grant Nos. 106-2113-M-002-022-MY3 and 107-2113-M-002-011-MY3. We thank Ms. C.-Y. Chien of Instrumentation Center at National Taiwan University for her assistance in the HR-TEM measurements.

Appendix A. Supplementary data

Supplementary data to this article can be found online at <https://doi.org/10.1016/j.jpowsour.2019.227470>.

References

- [1] M. Grätzel, J. Photochem. Photobiol. C Photochem. Rev. 4 (2003) 145–153.
- [2] B. O'Regan, M. Grätzel, Nature 353 (1991) 737–740.
- [3] D. Sengupta, P. Das, B. Mondal, K. Mukherjee, Renew. Sustain. Energy Rev. 60 (2016) 356–376.
- [4] S. Yun, A. Hagfeldt, T. Ma, Adv. Mater. 26 (2014) 6210–6237.
- [5] S. Hou, X. Cai, H. Wu, X. Yu, M. Peng, K. Yan, D. Zou, Energy Environ. Sci. 6 (2013).
- [6] B.E. Hardin, H.J. Snaith, M.D. McGehee, Nat. Photonics 6 (2012) 162–169.
- [7] M. Kouhnavard, N.A. Ludin, B.V. Ghaffari, K. Sopian, S. Ikeda, ChemSusChem 8 (2015) 1510–1533.
- [8] M. Wu, X. Lin, Y. Wang, L. Wang, W. Guo, D. Qi, X. Peng, A. Hagfeldt, M. Grätzel, T. Ma, J. Am. Chem. Soc. 134 (2012) 3419–3428.
- [9] F. Hao, P. Dong, Q. Luo, J. Li, J. Lou, H. Lin, Energy Environ. Sci. 6 (2013).
- [10] L. Kavan, J.H. Yum, M.K. Nazeeruddin, M. Grätzel, ACS Nano 5 (2011) 9171–9178.
- [11] H. Zheng, C.Y. Neo, X. Mei, J. Qiu, J. Ouyang, J. Mater. Chem. 22 (2012).
- [12] J.-F. Chen, Y. Mao, H.-F. Wang, P. Hu, ACS Catal. 6 (2016) 6804–6813.
- [13] S. Das, P. Sudhagar, V. Verma, D. Song, E. Ito, S.Y. Lee, Y.S. Kang, W. Choi, Adv. Funct. Mater. 21 (2011) 3729–3736.
- [14] M.-H. Yeh, C.-L. Sun, J.-S. Su, L.-Y. Lin, C.-P. Lee, C.-Y. Chen, C.-G. Wu, R. Vittal, K.-C. Ho, Carbon 50 (2012) 4192–4202.
- [15] Y. Xue, J. Liu, H. Chen, R. Wang, D. Li, J. Qu, L. Dai, Angew Chem. Int. Ed. Engl. 51 (2012) 12124–12127.
- [16] D.W. Zhang, X.D. Li, H.B. Li, S. Chen, Z. Sun, X.J. Yin, S.M. Huang, Carbon 49 (2011) 5382–5388.
- [17] J.D. Roy-Mayhew, D.J. Bozym, C. Punckt, I.A. Aksay, ACS Nano 4 (2010) 6203–6211.
- [18] J. Liang, Y. Jiao, M. Jaroniec, S.Z. Qiao, Angew Chem. Int. Ed. Engl. 51 (2012) 11496–11500.
- [19] J. Duan, S. Chen, M. Jaroniec, S.Z. Qiao, ACS Catal. 5 (2015) 5207–5234.
- [20] J. Tucek, P. Blonski, Z. Sofer, P. Simek, M. Petr, M. Pumera, M. Otyepka, R. Zboril, Adv. Mater. 28 (2016) 5045–5053.
- [21] C. Yu, Z. Liu, X. Meng, B. Lu, D. Cui, J. Qiu, Nanoscale 8 (2016) 17458–17464.
- [22] C.H. Choi, M.W. Chung, H.C. Kwon, S.H. Park, S.I. Woo, J. Mater. Chem. 1 (2013).
- [23] J.P. Paraknowitsch, A. Thomas, Energy Environ. Sci. 6 (2013).
- [24] S. Zhou, J. Xu, Y. Xiao, N. Zhao, C.-P. Wong, Nano Energy 13 (2015) 458–466.
- [25] C.A. Tseng, C.C. Chen, R.K. Ulaganathan, C.P. Lee, H.C. Chiang, C.F. Chang, Y. T. Chen, ACS Appl. Mater. Interfaces 9 (2017) 25067–25072.
- [26] L.M. Malard, M.A. Pimenta, G. Dresselhaus, M.S. Dresselhaus, Phys. Rep. 473 (2009) 51–87.

- [27] A.G. Kannan, J. Zhao, S.G. Jo, Y.S. Kang, D.-W. Kim, *J. Mater. Chem. A* 2 (2014) 12232–12239.
- [28] M.-Y. Yen, C.-K. Hsieh, C.-C. Teng, M.-C. Hsiao, P.-I. Liu, C.-C.M. Ma, M.-C. Tsai, C.-H. Tsai, Y.-R. Lin, T.-Y. Chou, *RSC Adv.* 2 (2012).
- [29] Y. Zhang, Z. Sun, H. Wang, Y. Wang, M. Liang, S. Xue, *RSC Adv.* 5 (2015) 10430–10439.
- [30] C.-A. Tseng, C.-P. Lee, Y.-J. Huang, H.-W. Pang, K.-C. Ho, Y.-T. Chen, *Mater. Today Energy* 8 (2018) 15–21.
- [31] S. Kundu, W. Xia, W. Busser, M. Becker, D.A. Schmidt, M. Havenith, M. Muhler, *Phys. Chem. Chem. Phys.* 12 (2010) 4351–4359.
- [32] W.-W. Wang, J.-S. Dang, X. Zhao, S. Nagase, *J. Phys. Chem. C* 120 (2016) 5673–5681.
- [33] X. Wang, J. Wang, D. Wang, S. Dou, Z. Ma, J. Wu, L. Tao, A. Shen, C. Ouyang, Q. Liu, S. Wang, *Chem. Commun.* 50 (2014) 4839–4842.

Supporting Information

N- and S-codoped graphene hollow nanoballs as an efficient Pt-free electrocatalyst for dye-sensitized solar cells

Yu-Ching Chang,^{a,†} Chi-Ang Tseng,^{a,†} Chuan-Pei Lee,^{b,†} Shiuan-Bai Ann,^c Yi-June Huang,^c Kuo-Chuan Ho,^c and Yit-Tsong Chen^{a,d,}*

^a Department of Chemistry, National Taiwan University, No. 1, Sec. 4, Roosevelt Road, Taipei 106, Taiwan

^b Department of Applied Physics and Chemistry, University of Taipei, Taipei 10048, Taiwan

^c Department of Chemical Engineering, National Taiwan University, Taipei 10617, Taiwan

^d Institute of Atomic and Molecular Sciences, Academia Sinica, P.O. Box 23-166, Taipei 106, Taiwan

*Address correspondence to: ytchem@ntu.edu.tw

† These authors contributed equally.

Section S1. Chemicals and Materials

Lithium iodide (LiI, synthetical grade) and iodine (I₂, synthetical grade) were obtained from Merck. Acetone (99+%), tert-butyl alcohol (tBA, 96%), guanidine thiocyanate (GuSCN, 99+%), and 4-tert-butylpyridine (TBP, 96%) were purchased from Acros. Ti (IV) tetraisopropoxide (TTIP, >98%), lithium perchlorate (LiClO₄, ≥98.0%), ethanol (EtOH, absolute), isopropanol (IPA, 99.5%), sulfuric acid (H₂SO₄, 95–97%), sulfur powder (99.98%), and 2-methoxyethanol (99.95%) were received from Sigma-Aldrich. Acetonitrile (ACN, 99.99%) was obtained from J. T. Baker. Cis-diisothiocyanato-bis (2,2'-bipyridyl-4,4'-dicarboxylato) ruthenium (II) bis(tetra-butylammonium) (N719 dye) and 1,2-dimethyl-3-propylimidazolium iodide (DMPII) were purchased from Solaronix (SA, Aubonne, Switzerland). Carbon cloth (CC, WOS1002, thickness: 360 μm, basic weight: 120 g cm⁻², sheet resistance: 0.63 Ω sq.⁻¹) was purchased from CeTech Co., Ltd., Taiwan. Cu foils (thickness: 25 μm, purity: 99.8%) were received from Alfa Aesar. Methane (CH₄, 99.9995%) and hydrogen (H₂, 99.9995%) were obtained from FMI gas Co. Ltd., Taiwan.

Section S2. The CVD syntheses of GHBs and heteroatoms-doped GHBs

S2.1. Synthesis of GHBs

The experimental details of synthesizing GHBs in chemical vapor deposition (CVD) reactions can be found in our previous publication.[S1] Shown in **Fig. S1** is a CVD system used to synthesize multilayer graphene-wrapped copper nanoparticles (MLG-CuNPs), in which the CuNP cores were subsequently etched away with Marble's reagent. In the CVD reaction, methane and hydrogen were applied as gaseous chemical precursors with the same flow rate of 200 sccm and total pressure of

2 torr. A quartz tube of 1 inch in diameter, located in a 40 cm long temperature-programmable furnace, was employed as the CVD reaction chamber with one end linked a gas inlet and the other end connected to a dry pump. A copper foil (1 cm \times 1 cm \times 25 μ m), used as the chemical precursor to form CuNPs in CVD reactions, was contained in a tungsten boat and placed at the center of the furnace. A carbon cloth (CC)-containing silicon wafer (1 cm \times 1 cm), used as a collection substrate, was put inside the quartz tube and located \sim 2.5 cm away from the furnace edge.

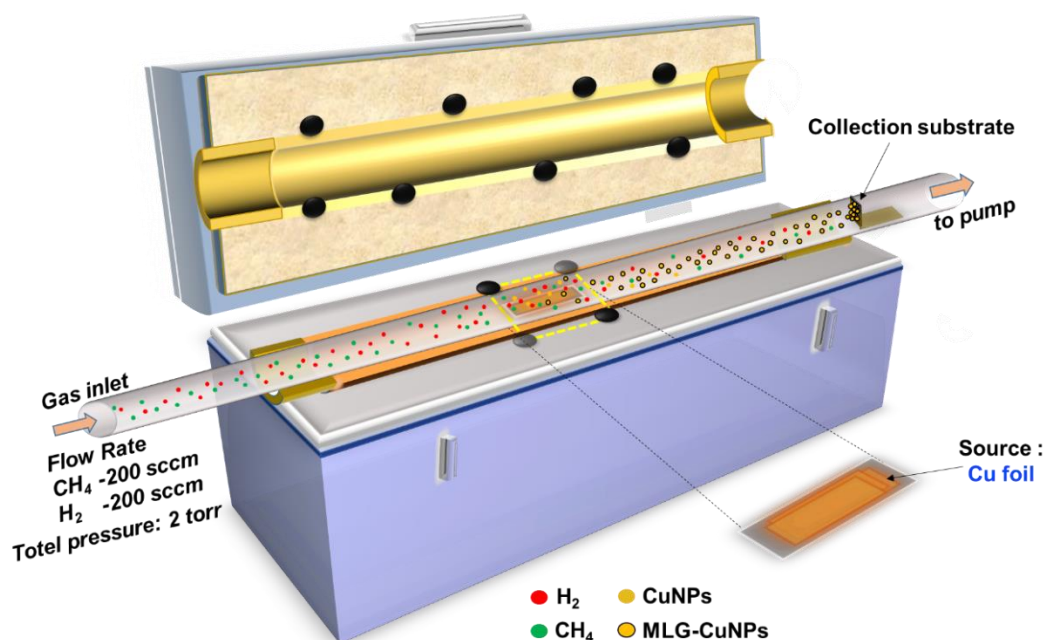


Fig. S1. A schematic representation for the CVD reaction to grow MLG-CuNPs. Subsequently, GHBs were obtained by etching away the CuNP cores of the as-synthesized MLG-CuNPs with Marble's reagent.

To produce MLG-CuNPs in CVD reactions, the furnace temperature was raised to 1090 $^{\circ}$ C to synthesize CuNPs, which could serve as a template for simultaneously catalyzing the formation of MLG on the CuNP surface. The as-synthesized vapor-phase MLG-CuNPs were carried by the gas flow to deposit onto a CC-containing substrate located at the low-temperature region (\sim 230 $^{\circ}$ C) for 2 hours.

We then washed the as-synthesized MLG-CuNPs with Marble's reagent to etch away the CuNP cores to obtain GHBs.

S2.2. Synthesis of N-GHBs

The synthetic protocols for N-GHBs in CVD reactions were the same as those of synthesizing GHBs described above in **Section S2.1**, except for adding melamine as the nitrogen source. The melamine powder was put in a tungsten boat, which was placed at 3 cm away from the furnace edge near the gas inlet as illustrated in **Fig. S2**.

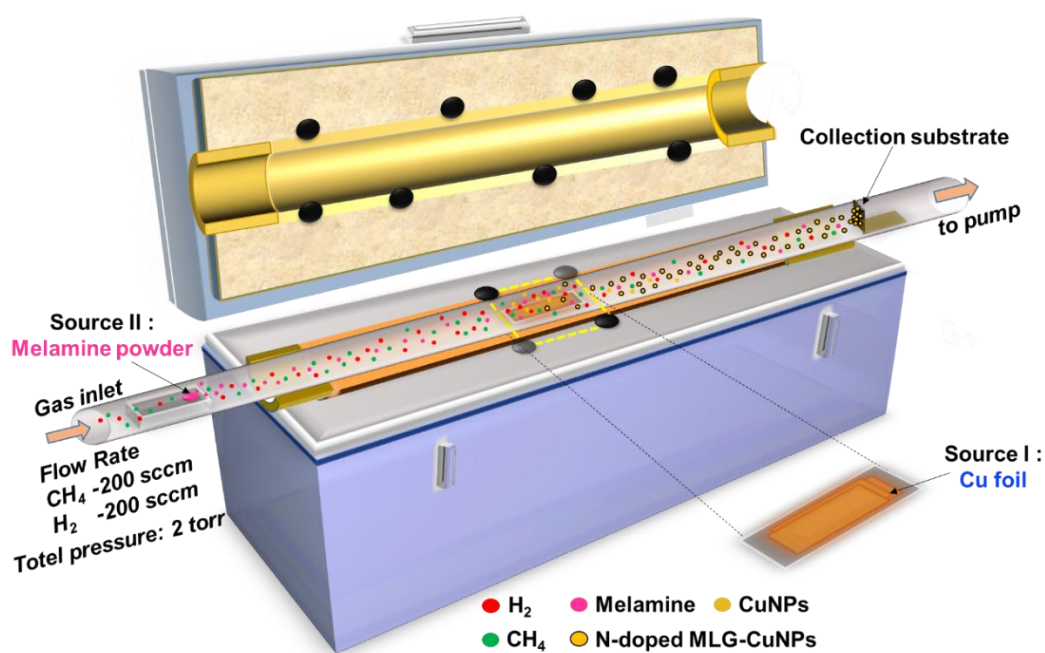


Fig. S2. A design illustrates the growth of N-GHBs in CVD reactions, in which melamine powder was used as a chemical precursor to dope N in GHBs.

S2.3. Synthesis of S-GHBs

For the synthesis of S-GHBs, we first synthesized GHBs via the CVD protocols described in **Section S2.1**. Subsequently, we put the as-synthesized GHBs sample in a

tungsten boat and then placed the boat at the center of the furnace. Sulfur powder was used as the sulfur source to be doped in GHBs. As illustrated in **Fig. S3**, the sulfur powder was contained in a tungsten boat, which was located 10 cm away from the furnace edge near the gas inlet. During the CVD reaction, while the sulfur powder was heated to 200 °C with a heating tape, the furnace temperature was raised up to 600 °C for growing S-GHBs.

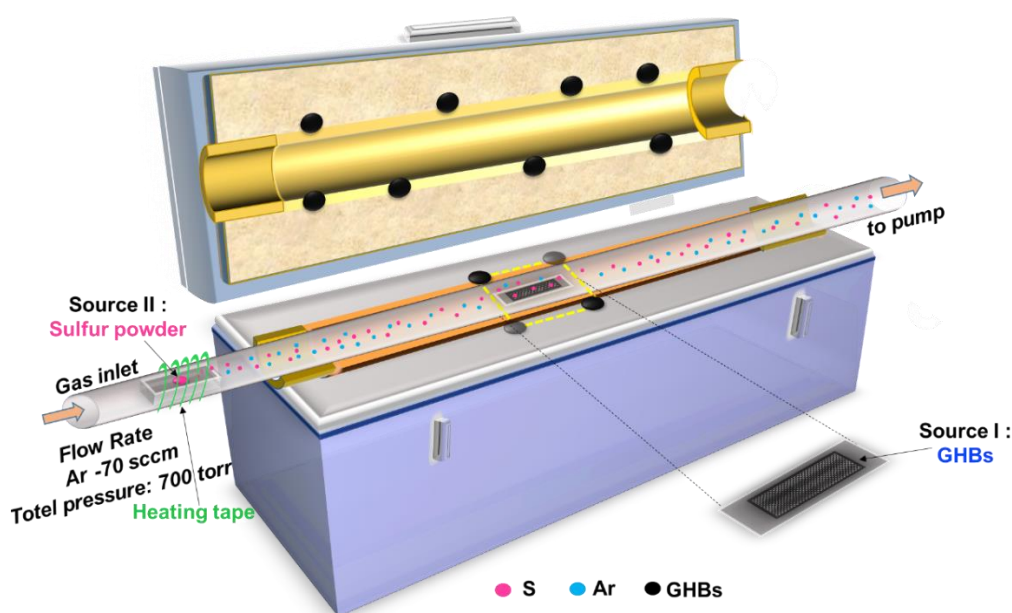


Fig. S3. A schematic representation shows the CVD design for growing S-GHBs. In the two-step synthetic reactions, after GHBs were grown in the first CVD reaction, the as-grown GHBs were then placed at the center of the furnace for the second CVD reaction. During the second CVD reaction, sulfur powder was used as the sulfur source to be doped for the formation of S-GHBs.

S2.4. Synthesis of N,S-GHBs

First, we grew N-GHB in the CVD reaction following the protocols described in **Section S2.2**. We then put the as-grown N-GHBs in a tungsten boat and placed the boat at the center of the furnace (**Fig. S4**). We added sulfur powder in a tungsten boat

and placed the boat at 10 cm away from the furnace edge near the gas inlet. In the following CVD reaction, while the sulfur powder was heated to 200 °C with a heating tape, the temperature of the furnace was raised up to 600 °C for growing N,S-GHBs.

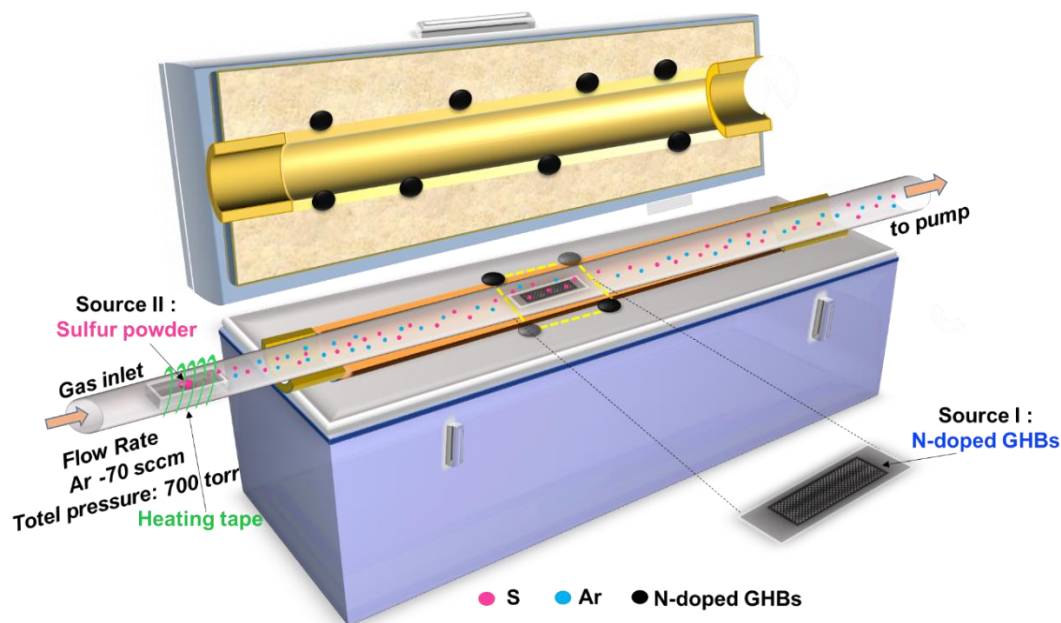


Fig S4. The production of N,S-GHBs was via two-step CVD reactions. In the first step, N-GHBs were grown in CVD reaction following the protocols of **Section S2.2**. In the second step, the as-synthesized N-GHBs were then put at the center of the furnace for another CVD reaction, where sulfur powder was used to dope S in N-GHBs for the formation of N,S-GHBs.

Section S3. Calculation of the crystallite size of graphene

The Raman spectrum of the as-synthesized GHBs is shown in **Fig. 1b** of the main text. It is well known that the intensity ratio of the D to G bands (I_D/I_G) is inversely related to the crystallite size of graphene and can be calculated from the Tuinstra-Koenig relationship[S2]

$$L_a \text{ (nm)} = 2.4 \times 10^{-10} \times \lambda^4 \times (I_D/I_G)^{-1}$$

where L_a and λ are the crystallite size of graphene and the wavelength of an incident laser, respectively. With the laser excitation at 488 nm, the I_D/I_G in the observed Raman spectrum of GHBs was measured to be 1.5. The corresponding crystallite size of ~9 nm in GHBs was calculated from the above formula.

Section S4. Preparation of CEs

The CC substrates were cleaned by soaking in a H_2SO_4 solution for one week, and then washed sequentially with deionized water, ethanol, and isopropanol. The as-synthesized GHBs/CC, N-GHBs/CC, S-GHBs/CC, and N,S-GHBs/CC were prepared respectively for different metal-free CEs to be used in DSSCs. In addition, a Pt catalytic layer was deposited on a cleaned CC substrate (denoted by sputtered Pt/CC) with a direct current (DC) sputtering method. The sputtered Pt/CC was employed as a standard CE in DSSCs.

Section S5. Fabrication of DSSCs

A TiO_2 photoanode was composed of a compact layer, a transparent layer, and a scattering layer on a fluorine-doped SnO_2 (FTO, TEC-7, $10 \Omega \text{ sq}^{-1}$, NSG America Inc., New Jersey, USA) conducting glass substrate. Before use, the FTO was cleaned with a neutral cleaner and then washed sequentially with deionized water, acetone, and isopropanol. Thereafter, a precursor solution containing tetraisopropoxide and 2-methoxyethanol (weight ratio = 1:3) was used to cover a compact layer (~100 nm in

thickness) on the cleaned FTO substrate by spin-coating to obtain a good mechanical contact between the conducting glass and TiO₂ film. A transparent TiO₂ layer (~10 μm in thickness) was coated on the compact layer via the doctor blade technique by using a commercial transparent TiO₂ paste (Ti-nanoxide HT/SP, an average diameter of ~13 nm, Solaronix).[S3] A scattering layer (~4 μm in thickness) was then coated on the transparent layer with the same doctor blade technique by using a home-made scattering paste. Before the next TiO₂ coating, each layer was sintered at 500 °C for 30 min in an ambient environment. The as-prepared TiO₂ electrode was immersed in a 500 μM N719 dye solution, containing a mixed solvent of acetonitrile and tert-butyl alcohol (volume ratio = 1:1), for 24 h at room temperature. Such a prepared dye-sensitized TiO₂ photoanode was coupled with a CE; these two electrodes were separated by a 60 μm-thick Surlyn[®] film (SX1170-60, Solaronix, SA, Aubonne, Switzerland). A mixture of 1.2 M DMPII, 0.35M I₂, 0.1 M GuSCN, and 0.5 M TBP in acetonitrile/3-methoxypropionitrile (volume ratio = 8:2) was used as the electrolyte.

Section S6. Measurements and instruments

S6.1. Electron microscopy of SEM, TEM, and EDS

The morphology of the as-prepared GHBs/CC, N-GHBs/CC, S-GHBs/CC, and N,S-GHBs/CC were characterized by field-emission scanning electron microscopy (FESEM, JEOL JSM 7600) equipped with an energy dispersive X-ray spectrometer (EDS) for elemental composition analysis. High-resolution TEM (HR-TEM) images were recorded with a field-emission transmission electron microscopy (FETEM, JEOL JEM-2100F) operating at an accelerating voltage of 300 kV.

S6.2. X-ray photoelectron spectroscopy

An X-ray photoelectron spectrometer (XPS, VG Scientific ESCALAB 250) was employed for chemical composition analysis. To avoid overlapping signals from the as-synthesized samples and a CC substrate, the XPS measurements were conducted by depositing the as-synthesized sample on a silicon wafer (with a 300 nm-thick SiO₂ dielectric layer). We calculated the doping levels of N- and/or S-doped GHBs/CC (i.e., N-GHBs/CC, S-GHBs/CC, and N,S-GHBs/CC) from the observed XPS data by

$$\text{element doping level} = \frac{A_2/ASF_2}{A_1/ASF_1 + A_2/ASF_2 + A_3/ASF_3} \times 100\%$$

where A is the integration area of the signal and ASF is the atomic sensitivity factor.

S6.3. DSSC

The surface of a DSSC was covered by a mask, leaving a light-illuminating area of 0.16 cm², and then illuminated by a class-A quality solar simulator (XES-301S, AM 1.5G, San-EI Electric Co., Ltd.) with the light intensity of 100 mW cm⁻². The incident light intensity (100 mW cm⁻²) was calibrated with a standard Si cell (PECSI01, Peccell Technologies, Inc., Yokohama, Japan). Photoelectrochemical characteristics of a DSSC were recorded with a potentiostat/galvanostat (PGSTAT 30, Autolab, Eco-Chemie, the Netherlands). Electrochemical impedance spectroscopy (EIS) was used to investigate the interfacial charge transfer kinetics for the electrocatalytic electrodes by using a symmetric cell, consisting of the same electrocatalyst on both anode and cathode. The FRA2 module was operated between 10 mHz and 100 kHz under an open-circuit condition, with an AC amplitude of ±10 mV. The data of impedance spectra were analyzed by fitting them into an equivalent circuit model, using Z-view software.[S4] The incident photon-to-electron conversion

efficiency (IPCE) curves were obtained at the short-circuit condition. The light source was a class-A quality solar simulator (PEC-L11, AM1.5G, Peccell Technologies, Inc.) and was focused through a monochromator (74100, Oriel Instrument, California, USA) onto the photovoltaic cell. The monochromator was incremented through the visible spectrum to generate the IPCE (λ) as defined below

$$\text{IPCE}(\lambda) = 1240 (J_{\text{SC}}/\lambda\phi)$$

where λ is the wavelength, J_{SC} is the short-circuit photocurrent density (mA cm^{-2}) recorded with a potentiostat/galvanostat, and ϕ is the incident radiative flux (W m^{-2}) measured with an optical detector (818-SL, Newport, California, USA) and a power meter (1916-R, Newport, California, USA).

Cyclic voltammetry (CV) was performed to investigate the electrocatalytic abilities of the tested CEs. The CV was carried out with a three-electrode electrochemical system by using an electrode (i.e., bare CC, GHB/CC, N-GHB/CC, S-GHBs/CC, N,S-GHBs/CC, or sputtered Pt/CC) as the working electrode, a Pt foil as the CE, and an Ag/Ag⁺ electrode as the reference electrode in an acetonitrile solution, containing 10 mM I⁻, 1 mM I₂, and 0.1 M LiClO₄.

Section S7. Literature review

Table S1 summarizes the DSSC performances of a N,S-GHBs/CC CE and other previously reported electrodes. The promising results of open-circuit voltage (V_{oc}) and fill factor (FF) indicate that the N,S-GHBs/CC CE exhibits better electrocatalytic ability toward the triiodide reduction reaction with a faster charge-transfer process.

Table S1. Comparison of the DSSC performances of various counter electrodes.

Counter electrodes	η (%)	V_{oc} (mV)	J_{sc} (mA/cm ²)	FF	Reference
3D graphene	8.46	713	17.20	69	S5
N-doped graphene nanoplatelets	9.05	883	13.83	74	S6
N-doped graphene	4.75	820	10.55	55	S7
P-doped reduced graphene oxide	6.04	740	15.50	53	S8
N,P-codoped graphene	8.57	770	15.91	69	S9
N,S-codoped graphene	7.42	700	16.78	62	S10
N,S-codoped reduced graphene oxide	4.73	601	11.70	67	S11
N,S-codoped graphene networks	9.40	744	16.86	74	S12
N,S-GHBs	9.02	798	15.71	72	This work

Reference

- [S1] C.-A. Tseng, C.-P. Lee, Y.-J. Huang, H.-W. Pang, K.-C. Ho, Y.-T. Chen, *Materials Today Energy*, 8 (2018) 15-21.
- [S2] L.G. Cançado, K. Takai, T. Enoki, M. Endo, Y.A. Kim, H. Mizusaki, A. Jorio, L.N. Coelho, R. Magalhães-Paniago, M.A. Pimenta, *Applied Physics Letters*, 88 (2006).
- [S3] I.T. Chiu, C.-T. Li, C.-P. Lee, P.-Y. Chen, Y.-H. Tseng, R. Vittal, K.-C. Ho, *Nano Energy*, 22 (2016) 594-606.
- [S4] L.-Y. Chang, C.-T. Li, Y.-Y. Li, C.-P. Lee, M.-H. Yeh, K.-C. Ho, J.-J. Lin, *Electrochimica Acta*, 155 (2015) 263-271.
- [S5] H.J. Ahn, I.H. Kim, J.C. Yoon, S.I. Kim, J.H. Jang, *Chem Commun*, 50 (2014) 2412-2415.
- [S6] M.J. Ju, J.C. Kim, H.J. Choi, I.T. Choi, S.G. Kim, K. Lim, J. Ko, J.J. Lee, I.Y. Jeon, J.B. Baek, H.K. Kim, *ACS Nano*, 7 (2013) 5243-5250.
- [S7] M.-Y. Yen, C.-K. Hsieh, C.-C. Teng, M.-C. Hsiao, P.-I. Liu, C.-C.M. Ma, M.-C. Tsai, C.-H. Tsai, Y.-R. Lin, T.-Y. Chou, *RSC Advances*, 2 (2012) 2725-2728.
- [S8] Z. Wang, P. Li, Y. Chen, J. He, J. Liu, W. Zhang, Y. Li, *Journal of Power Sources*, 263 (2014) 246-251.
- [S9] C. Yu, Z. Liu, X. Meng, B. Lu, D. Cui, J. Qiu, *Nanoscale*, 8 (2016) 17458-17464.

[S10] A.G. Kannan, J. Zhao, S.G. Jo, Y.S. Kang, D.-W. Kim, *J. Mater. Chem. A*, 2 (2014) 12232-12239.

[S11] Q. Luo, F. Hao, S. Wang, H. Shen, L. Zhao, J. Li, M. Grätzel, H. Lin, *The Journal of Physical Chemistry C*, 118 (2014) 17010-17018.

[S12] Z. Yu, Y. Bai, Y. Wang, Y. Liu, Y. Zhao, Y. Liu, K. Sun, *Chemical Engineering Journal*, 311 (2017) 302-309.